

Trends of Atlantic Wave Extremes as Simulated in a 40-Yr Wave Hindcast Using Kinematically Reanalyzed Wind Fields

XIAOLAN L. WANG* AND VAL R. SWAIL

Climate Research Branch, Meteorological Service of Canada, Downsview, Ontario, Canada

(Manuscript received 6 March 2001, in final form 13 August 2001)

ABSTRACT

In this study, seasonal extremes of wave height in the North Atlantic are analyzed. The analysis is based on a 40-yr (1958–97) numerical wave hindcast using an intensive kinematic reanalysis of wind fields. Changes in the ocean wave extremes are identified by performing the Mann–Kendall test, and are further related to changes in the atmospheric circulation (sea level pressure) by means of redundancy analysis. The relationship between sea level pressure and ocean wave extremes is also used to reconstruct the seasonal wave statistics for the last century (back to 1899).

Consistent with previous studies, this high-resolution Atlantic wave hindcast also shows that the northeast North Atlantic Ocean has experienced significant multidecadal variations in the last century, and it has indeed roughened in winters of the last four decades. The winter wave height increases are closely related to changes in the North Atlantic oscillation during the last four decades.

While showing trend patterns similar to the ones identified from a previous global wave hindcast using the NCEP reanalysis wind fields, this detailed Atlantic hindcast shows more significant increases in the region off the Canadian coast in summer and fall; and in winter it shows higher rates of increases in the region northwest of Ireland but less significant changes in the North Sea and in the region off the Scandinavian coast.

1. Introduction

There is a wide range of applications that require information on ocean wind and wave climate, its variability, and possible trend. Such applications include the determination of engineering design parameters for offshore oil and gas exploration, production, and transportation; coastal development; the detailed planning of shipping routes; and scientific requirements in areas such as climate research, in particular relating to potential anthropogenically induced changes in storm frequency and severity.

In the early 1990s, Bacon and Carter (1991, 1993) raised the issue of wave climate changes in the North Atlantic and North Sea by presenting a review of all available data describing long-term trends in the wave climate, using both visual estimate and instrumental measurements of wave height. They found that there exists an increase in mean wave height over the whole of the North Atlantic, possibly since 1950, of about 2%

yr^{-1} , and that the long-term changes in wave climate is linked to the atmospheric pressure gradient measured between the Iceland low and the Azores high.

In recent years there have been several attempts to investigate the variability of waves and storms in the North Atlantic Ocean. These are described in some detail by Wang and Swail (2001), but warrant a brief discussion here for historical context and comparison with the present study. The parameters of these studies are summarized in Table 1. The first of these studies was carried out by Kushnir et al. (1997), who generated a statistical hindcast to quantitatively estimate the systematic increase in wave heights over the period 1962–86. They found that an increasing trend in significant wave height (SWH) at several northeast Atlantic locations since 1960 or so was related to the systematic deepening of the Icelandic low and intensification of the Azores high over the last three decades. Their analysis also suggested that wave height south of 40°N has decreased during the same period. Subsequently, a major effort was undertaken by the European Union Waves and Storms in the Atlantic (WASA) project (WASA Group 1998; Gunther et al. 1998), which produced comprehensive estimates of linear trends in means and extremes of annual significant wave heights. Unfortunately, inhomogeneities and other problems with the hindcast in the area west of 20°W limited the reliability of the analysis to the extreme eastern North Atlantic, where it was

*Current affiliation: Monitoring Science and Strategies Division, Atmospheric Monitoring and Water Survey Directorate, Meteorological Service of Canada, Downsview, Ontario, Canada.

Corresponding author address: Dr. Xiaolan L. Wang, AMWSD, Meteorological Service of Canada, 4905 Dufferin St., Downsview, ON, M3H 5T4 Canada.
E-mail: Xiaolan.Wang@ec.gc.ca

TABLE 1. Comparison of recent wave climatology studies.

| | Kushnir et al. (1997) | WASA Group (1998) | Sterl et al. (1998) | Wang and Swail (2001) | This study |
|---------------------|--|---|-------------------------------------|--|--|
| Area | North Atlantic (0°–70°N) | Northeast Atlantic (38°–77°N, 30°W–45°E) | Global | NH | North Atlantic (20°–70°N, 80°W–20°E) |
| Period | 1980–89 | 1955–94 | 1979–93 | 1958–97 | 1958–97 |
| Grid resolution | 2.5° lat–lon | 0.5° lat by 0.75° lon for Northeast Atlantic nest | 1.5° and 3.5° lat–lon | 1.25° lat × 2.5° lon | 0.625° lat × 0.833° lon |
| Wind input | Operational: 12-h ECMWF 1000-hPa wind | Operational: 6-h FNMOC* 10-m surface wind plus 6-h DNMI** 10-m surface wind | Reanalysis: 6-h ERA-15 surface wind | Reanalysis: 6-h NRA-40 surface wind | Reanalysis: 6-h NRA-40 10-m surface wind with kinematic analysis |
| Wave model | Oceanweather 1G | WAM 3G | WAM 3G | Oceanweather 2G | Oceanweather 3G |
| Analysis methods | Canonical correlation analysis; least squares linear trend | Least squares linear trend; redundancy analysis | Linear trend with Student's t test | Linear trend with Mann–Kendall test; redundancy analysis | Linear trend with Mann–Kendall test; redundancy analysis |
| Statistics analyzed | Monthly means | Annual maxima, means, 90th and 99th percentiles; monthly 50th, 80th, 90th percentiles | Monthly means | Seasonal 90th and 99th percentiles | Seasonal 90th and 99th percentiles |

* Fleet Numerical Meteorology and Oceanography Center.
 ** Norwegian Meteorological Institute.

concluded that the wave climate has undergone significant variations on a timescale of decades. Part of that variability was found to be related to the North Atlantic Oscillation (NAO). In spite of an apparent artificial worsening of the storm climate in data-sparse areas (Gunther et al. 1998), the WASA hindcast produced a well-validated reconstruction of the wave climate of the northeast Atlantic based on the best information and technology available at that time.

The advent of long-term climate reanalysis projects undertaken by major numerical weather prediction centers significantly changed the approach to the investigation of climate variability, and to a lesser extent trend, on decadal and longer timescales. Inhomogeneities associated with improvements in data analysis techniques, and evolution and upgrades in operational numerical models have led these centers to major attempts to produce a consistent analysis of the atmosphere through so-called reanalysis using historical atmospheric observations and current analysis schemes and NWP models. Reanalysis does not account for changes in time of data sources, density, or quality, thus leaving some unknown degree of temporal inhomogeneity. Two such projects have been widely used for a variety of climate research applications: 1) a preliminary global atmospheric reanalysis produced at the European Centre for Medium-Range Weather Forecasts (ECMWF) for the 15-yr period from 1979 to 1993 [ECMWF reanalysis (ERA-15); Gibson et al. 1996]; and 2) the National Centers for Environment Prediction–National Center for Atmospheric Research (NCEP–NCAR) reanalysis project (hereafter NRA; Kalnay et al. 1996).

The first wave-climate study using reanalysis data was undertaken by Sterl et al. (1998), who analyzed the linear trend of the monthly mean SWH for each calendar month over the 15-yr ERA period. Large trends were found in January in the North Atlantic mean SWH, and in July in the ocean south of Africa; the trends were found to vary greatly from month to month. While the Sterl et al. (1998) hindcast represented a major advance in wind field quality and homogeneity, the time period was too short to confirm a significant change in the global wave climate.

The initial NRA reanalysis covered a much longer 40-yr period. The first 40-yr wave hindcast based on reanalysis products was a global study carried out by Environment Canada (Cox and Swail 2001), which was subsequently analyzed for trend and variability by Wang and Swail (2001, hereafter WS01). This global hindcast showed very good agreement with observations across the North Atlantic up to the 99th percentiles of SWH. WS01 analyzed seasonal extremes of SWH in terms of the 90th and 99th percentiles. They first used the Mann–Kendall test to assess linear trends of SWH extremes on seasonal timescales, accounting for the effect of autocorrelation when assessing trends and their significance level. They then used redundancy analysis (RA) technique to characterize the links between the large-

scale variability of SWH extremes and large-scale atmospheric circulation [sea level pressure (SLP)] patterns, which are further used to extend the numerical hindcast back to January 1899, providing a best guess of the historical variability of SWH extremes. Significant increases in the northeast North Atlantic were found in the winter [January–March (JFM)] season for the last four decades, matched by significant decreases in the subtropical North Atlantic. These trends were found to be closely connected to significant changes in the variability of the NAO. Based on the statistical hindcast, however, no significant trends in SWH extremes were found for the last century, although long-term variability was pronounced (the upward trend in the last four decades is matched by a downward trend in the previous decades).

It is difficult to quantitatively compare the estimates from the various studies done to date, since they cover different time periods, somewhat different areas, and different wave statistics. However, it is notable that all the studies show a marked increase in SWH in the northeast North Atlantic, although the magnitudes of the trend, and variability, differ considerably.

In parallel with the initial NRA-based global wave hindcast, a detailed high-resolution wave hindcast was produced for the North Atlantic (Swail and Cox 2000). The objective of that project was to produce an engineering-quality, homogeneous, long-term wind and wave database for assessment of the wave climate of the North Atlantic, its trend and variability. The most important feature of the hindcast was the rigorous attention devoted to producing the wind fields used to drive the wave model. To remove potential biases in the historical wind fields, all wind observations from ships and buoys were reassimilated into the analysis taking account of the method of observation, anemometer height, and stability. Wind fields for all significant storms were then painstakingly kinematically reanalyzed. Furthermore, high-resolution surface wind fields for all tropical cyclones, as specified by a proven tropical cyclone boundary layer model, were assimilated into the wind fields to provide greater skill and resolution in the resulting wave hindcasts. Finally, these high-quality wind fields were used to force a much higher-resolution, third generation wave model.

The purpose of the present study is twofold. We will verify whether or not our detailed North Atlantic wave hindcast (referred to as “the Atlantic hindcast” hereafter), which uses a different (high resolution, 3G) wave model forced by the most rigorously kinematically analyzed wind field we can produce, leads to conclusions similar to those of previous studies. In particular, the wave hindcast has been shown to make significant improvement in resolving the most extreme storms, including tropical storms (Swail and Cox 2000). We use the Mann–Kendall test to identify trends in seasonal SWH extremes and we use the RA technique to link the large-scale variability of ocean waves with large-scale

atmospheric circulation regimes. We will also assess the homogeneity of the wave data. We use the RA regression model, trained with detrended SLP and SWH data, to “predict” SWH extremes using the “undetrended” SLP. Then, we compare trends in the RA-predicted SWH extremes with the corresponding ones estimated directly from the Atlantic (numerical) hindcast. Consistent trends suggest that the wave data is of the same degree of homogeneity as the SLP data.

In section 2, we give a brief description of the wave hindcast model and hindcast methodology, particularly the modifications of the surface wind fields; we also compare our Atlantic wave hindcast with previous studies in this field. Section 3 briefly describes the statistical analysis procedures used in this study. We then present and discuss the results of our trend analysis in section 4, and we briefly discuss the homogeneity of wave data in section 5. Section 6 relates the ocean wave variability with atmospheric circulation patterns. Finally, we complete this paper with a summary in section 7.

2. The North Atlantic wave reanalysis

a. Wave model

The wave hindcast was carried out using a discrete spectral type wave model called OWI 3G. In this model, the spectrum is resolved at each grid point in 24 directional bins and 23 frequency bins. A fine mesh grid spacing of 0.625° latitude \times 0.833° longitude was used over the whole grid domain from 0° – 75.625° N to 20° E– 80° W. The wave model was run with deepwater physics throughout, and was driven by the final kinematically reanalyzed wind fields as described in the next section. This wave model has been shown to reproduce observed wave heights very well when driven by accurate wind fields (Cardone et al. 1995, 1996). Further details on the wave model are given in the appendix.

b. Wind fields

The most important, and unique, element of this Atlantic hindcast was the enormous effort devoted to producing the wind fields for the wave model; this effort accounted for more than 10 000 meteorologist hours of effort spent in manual and interactive kinematic analysis. Details of the wind field generation are given in Swail and Cox (2000); however, a brief description will be included here for completeness.

In the first step of the wind field generation, the 6-hourly NRA surface (10 m) winds are used as a background field, after first being converted to an equivalent neutral wind using the NRA 2-m surface temperature and sea surface temperature fields and the algorithm described by Cardone et al. (1990).

In the second step of the wind analysis, all available historical marine surface data, including buoy observations, ship reports, coastal stations, and *ERS-1/2* scat-

terometer winds are displayed in the Wind WorkStation graphical interface. The in situ measured wind and wave data came from a variety of sources. The U.S. buoy and Coastal Marine Automated Network (C-MAN) data came from the National Oceanic and Atmospheric Administration (NOAA) Marine Environmental Buoy database on CD-ROM; the Canadian buoy data came from the Marine Environmental Data Service marine CD-ROM; and the remaining data came from the Comprehensive Ocean–Atmosphere Data Set (COADS; Woodruff et al. 1987). The *ERS-1/2* scatterometer measurements were extracted from Ifremer's CD-ROM set using the recommended quality controls, and then spatially binned onto the wave model grid every 6 h using a ± 3 -h window.

A crucial feature of the Atlantic hindcast concerns the treatment of these surface observations. The NRA assimilation scheme (as with most numerical weather prediction schemes) treated all observations at a 10-m reference level, whereas ship and drilling platform observations may actually range from about 15 to more than 100 m, and buoy observations are typically taken about 5 m. Over the 40-yr duration of the NRA this may introduce biases similar to those found by Cardone et al. (1990) due to the increasing heights of shipboard anemometers and the higher fraction of wind measurements compared to wind estimates. To overcome any potential bias in this project, all surface wind data were first adjusted to effective neutral 10-m winds following the approach described in Cardone et al. (1996).

It was found that tropical storms are poorly resolved in the NRA wind fields. Thus, in the third step of the wind analysis, high-resolution surface wind fields for all tropical cyclones, as specified by a proven tropical cyclone boundary layer model (Cardone et al. 1994; Thompson and Cardone 1996), are assimilated into the wind fields to provide greater skill and resolution in the resulting wave hindcasts. Track and initial estimates of intensity are taken, with some modification, from the NOAA Tropical Prediction Center's (TPC) HURDAT database. The radius of maximum wind is determined using a pressure profile fit to available surface observations and aircraft reconnaissance data. Reconnaissance data are taken from TPC's Annual Data and Verification Tabulation diskettes from 1989 to 1996, digitally scanned from manuscript records for the period 1974–88, and manually scanned from reconnaissance microfilm for periods prior to 1974. Surface winds generated from the model are then evaluated against available surface data and aircraft reconnaissance wind observations adjusted to the surface (10 m) as described by Powell and Black (1990). Model winds within 240 nautical miles from the center are then exported on a higher-resolution 0.5° latitude–longitude grid for inclusion and blending using the Wind WorkStation.

The fourth, and most labor-intensive and time-consuming, but also the most important step, was the detailed kinematic analysis incorporating all of the wind

information noted above. The interactive wind analysis methodology used follows that used in previous hindcast studies (Cardone et al. 1995, 1996). Particular attention is spent on strong extratropical systems, blending tropical model winds into the NCEP surface wind field, and in the quality control of surface data. Kinematically analyzed winds from previous hindcasts of severe extratropical storms in the northwest Atlantic (Swail et al. 1995) are incorporated into the present analysis on the North Atlantic wave model grid.

As an integral part of step 4 above, altimeter wave measurements are used in an inverse modeling approach as follows. Hindcast wave heights over the North Atlantic Ocean derived from the global 2G model (Cox and Swail 2001) are compared to altimeter wave measurements. Areas where the resulting wave fields are deficient, as indicated by the altimeter, are brought to the analyst's attention and the analyst subjectively rectifies the deficiencies in the backward space–time evolution of the NRA wind field causing the discrepancy. Altimeter data came from both *ERS-1/2* and *TOPEX/Poseidon* instruments. The *ERS-1/2* altimeter measurements were extracted from Ifremer's CD-ROM set using the recommended quality controls, and then spatially binned onto the wave model grid every 6 h using a ± 3 -h window. TOPEX data was treated much the same as the ERS data, and the wave measurements from both instruments were adjusted as recommended by Cotton and Carter (1994).

All of the wind information, including the NRA background fields, the in situ and satellite measurements, the high-resolution tropical storm wind fields, and the manual kinematic analysis, were blended using the Interactive Objective Kinematic Analysis (IOKA) algorithm (Cox et al. 1995). In this technique, quadratic forms are fitted to the velocity components and wind speed separately, minimizing the differences between the analysis and the observations in the least squares sense. Separate weights are assigned to each class of observation. Final wind fields for each month were interpolated onto the 0.625° by 0.833° latitude–longitude wave model grid and then time interpolated to a 1-h time step.

c. Hindcast comparison, validation, and analysis

For the significant wave heights (SWH) measured at the Seven Stones light vessel, Carter and Draper (1988) reported a 3.4 cm yr^{-1} increase in the annual means of SWH during 1962–85. Bacon and Carter (1991) reported a 2.2 cm yr^{-1} increase in the annual means for 1962–85. Correspondingly, our Atlantic wave hindcast shows much smaller increases (of 0.05 – 0.21 cm yr^{-1} for the same period) at the three grid points (49.375°N and 5.8333°W , 50°N and 6.6667°W , 50.625°N and 5.8333°W) near the Seven Stones light vessel. Statistically, these changes are not significant even at 20% level. Changes in the annual maxima of SWH at these grid points are also found to be insignificant.

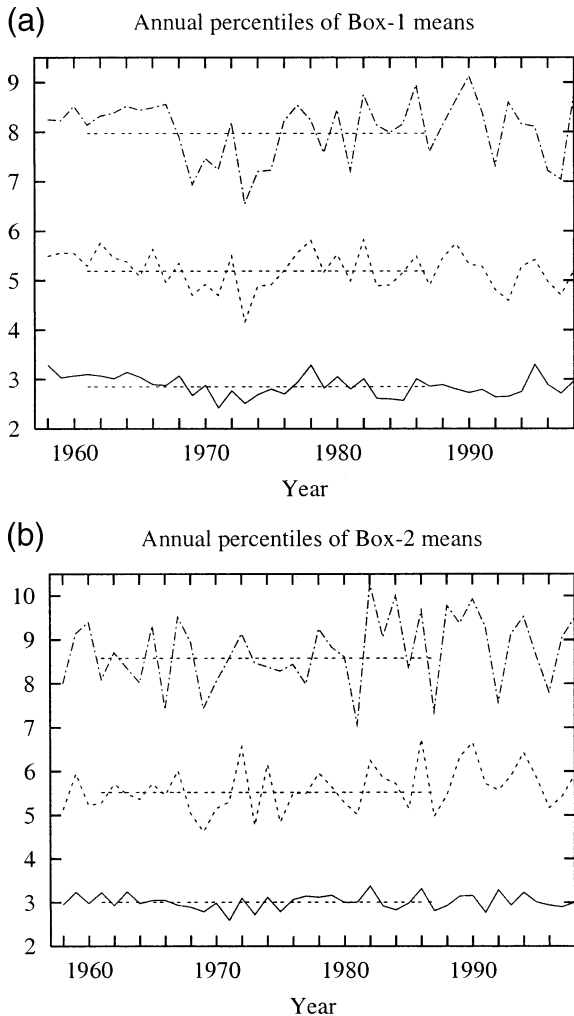


FIG. 1. Time series of the upper 1st, 10th, and 50th percentiles (from top to bottom) of the annual distribution of the area mean SWH for (a) Box-1 (50° – 55° N, 50° – 40° W) and (b) Box-2 (50° – 55° N, 20° – 10° W; cf. Bouws et al. 1996). The trend lines (straight dashed lines) are replaced by the long-term mean lines if they are not statistically significant at the 20% level.

Bouws et al. (1996) reported that the typical rate of increase for the 50th percentiles of the mean wave heights for Box-1 (50° – 55° N, 50° – 40° W) and Box-2 (50° – 55° N, 20° – 10° W) during 1961–87 are 2.3 and 2.7 cm yr^{-1} , respectively. The corresponding rate of changes in our Atlantic wave hindcast are -1.0 and 0.1 cm yr^{-1} ; no increases are found to be of any statistical significance (cf. Fig. 1). The discrepancy is mainly due to the fact that, during the first two decades (1960s and 1970s), the statistics in Bouws et al. (1996, see their Fig. 2) have much smaller values than the corresponding ones from the Atlantic hindcast. Their data from wave charts very likely underestimate the wave heights for this period.

The WASA wave hindcast (Gunther et al. 1998) shows increases of 0.25–0.75, 2–3, 3–4, and 7–10

cm yr^{-1} , respectively for the annual means, 90th and 99th percentiles, and maxima of northeast Atlantic SWH during 1955–94. Correspondingly, the Atlantic hindcast shows that during 1958–97 the northeast North Atlantic experienced increases of 0.5–2.5, 1–3, 2–6, and 4–7.6 cm yr^{-1} for the annual means, 90th and 99th percentiles, and maxima of SWH, respectively (cf. Fig. 2). The upper bounds of increase are 3.7, 3.6, 7.7 and 9.3 cm yr^{-1} for the 1958–94 period. Apparently, our Atlantic hindcast shows higher rates of increase in the annual means and 99th percentiles, while the increases in the annual maxima and 90th percentiles are of the same order as those estimated from the WASA wave hindcast. Note that it is not possible for us to do the comparison for exactly the same period, since we do not have wave hindcasts for 1955–57.

Gunther et al. (1998) also reported increases of 3.8, 2.7, 3.8, and 3.0 cm yr^{-1} for the annual maxima, 99th, 90th, and 50th percentiles of the Box-2 maximum significant wave heights from ship routing charts for 1961–87 (see their Table 2); and the corresponding increases in the WASA wave hindcast are 5.48, 1.01, 0.54, and 1.01 cm yr^{-1} (see their Table 3). The Atlantic hindcast shows no corresponding increases of statistical significance for either the 1961–87 period or the 1958–97 period (cf. Table 2). Moreover, the long-term means of the statistics from the Atlantic hindcast are smaller than the corresponding ones from the WASA wave hindcast, but greater than those of the ship charts (cf. Table 2).

At the Ocean Weather Station (OWS) Mike (66° N, 3° E), the WASA wave hindcast suggested that the annual maxima of SWH experienced an increase of 8.39 cm yr^{-1} in the period 1955–94 (see Table 7 in Gunther et al. 1998), and of 17 cm yr^{-1} in the period 1975–94. Grevemeyer et al. (2000) provided microseismological evidence that supports a worsening of the northeast Atlantic wave climate over the last two decades. Our wave reanalysis shows that the annual maxima at the grid point AE007927 (66.25° N, 3.3333° E), which is the grid point nearest the OWS Mike, had an increase of 5.0, 5.8, and 6.0 cm yr^{-1} for the periods 1958–97, 1958–94, and 1975–94, respectively (cf. Fig. 3). The increasing trend is highly statistically significant for both the 1958–97 and 1958–94 periods, but it is statistically insignificant for the 1975–94 period. Although a comparison for exactly the same 40-yr period is not possible here, there is clear evidence that the Atlantic hindcast shows lower rates of increase near the OWS Mike than does the WASA wave hindcast.

The Atlantic wave hindcast was exhaustively evaluated against both in situ (buoys and oil platforms) data and satellite altimeter waves. The evaluation is described in detail by Swail and Cox (2000) and Cox et al. (2001). The results showed excellent agreement with both altimeter and in situ data, not only at the 90th and 99th percentiles, but also with respect to the absolute extremes used in the generation of long-return period statistics. The North Atlantic wave reanalysis can truly

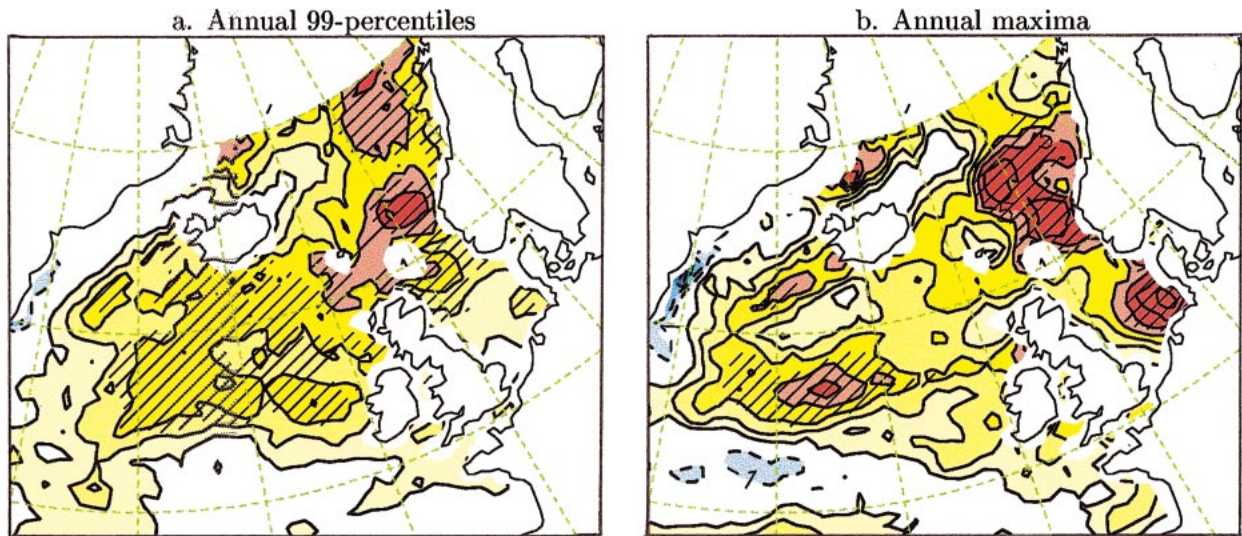


FIG. 2. Changes (cm yr^{-1}) of the annual 99th percentiles and maxima of SWH in the northeast North Atlantic. The contour interval is 1.0 cm yr^{-1} . Solid and dashed lines are positive and negative contours, respectively (zero contours are not drawn). Hatching indicates areas of significant changes (at the 5% level).

be considered an engineering-quality dataset, as confirmed in several proprietary oil industry studies in areas ranging from the Scotian shelf to the northeast Atlantic (V. J. Cardone 2001, personal communication).

The seasonal extremes of SWH, as simulated in the Atlantic hindcast, are analyzed for trends in this study. The seasonal extremes (90th and 99th percentiles) of SWH are derived from 6-hourly data on a 0.625° latitude \times 0.833° longitude grid over the North Atlantic (20° – 70°N , 80°W – 20°E). Then, the variability of SWH extremes is further linked to large-scale atmospheric circulation regimes by means of redundancy analysis. Here, the atmospheric circulation is represented by seasonal means of the NRA sea level pressure (SLP) for the North Atlantic sector (20° – 70°N , 80°W – 20°E), which are on a 2.5° latitude \times 2.5° longitude grid and cover the same 40-yr period (1958–97) as the wave hindcast. In order to produce a best guess of ocean wave statistics for the last century, the 1899–1997 seasonal means of SLP from the NCAR dataset ds010.1 (Trenberth and Paolino 1980) are also used in this study. The later SLP dataset is on a 5° latitude \times 5° longitude grid.

3. Methodologies and procedures

a. Methodologies

As in Wang and Swail (2001; hereafter WS01), the trend analysis in this study is carried out by fitting the following model to a time series Y_t :

$$Y_t = a + bt + R_t, \quad (1)$$

where a and b are regression parameters, and R_t is a red noise process with lag-1 autocorrelation c , that is, $R_t = cR_{t-1} + \varepsilon_t$, where ε_t denotes a white noise process. We decided to remove only the effect of lag-1 autocorrelation, because at lag >1 season few partial autocorrelations of the seasonal time series in question are statistically significant at the 5% level (approximately). Specifically, the time series Y_t is replaced by the series $W_t = (Y_t - cY_{t-1})/(1 - c)$, which is considerably less plagued by serial correlation and has the same slope parameter b as does the original time series Y_t . Since the effect of autocorrelation is negligible when the autocorrelation $c \leq 0.05$ (von Storch and Navarra 1995), we prewhiten the time series only when its $c > 0.05$.

TABLE 2. The changes and long-term means of annual statistics (maxima, 99th, 90th, and 50th percentiles) of the Box-2 maximum SWH during the 1961–87 and 1958–97 periods, as simulated in the Atlantic hindcast. The 80%, 90%, and 95% critical values of the Z-statistic are 1.282, 1.645, and 1.960, respectively. For easy comparison, the long-term means from the WASA wave hindcast and from ship charts are also given in brackets.

| | Period 1961–87 | | | | Period 1958–97 | | | |
|------------------------------|----------------|---------|--------|--------|----------------|-------|------|-------|
| | Max | 99th | 90th | 50th | Max | 99th | 90th | 50th |
| Change yr^{-1} (cm) | 0.83 | 2.50 | 0.67 | −0.09 | 0.34 | 1.71 | 1.14 | 0.00 |
| Z-statistic | 0.50 | 0.81 | 0.33 | −0.19 | 0.40 | 1.12 | 1.43 | −0.02 |
| Mean (m) | 13.39 | 11.28 | 7.11 | 3.95 | 13.66 | 11.39 | 7.06 | 3.96 |
| Mean (m; WASA) | (17.42) | (13.04) | (8.43) | (4.50) | | | | |
| Mean [m; ship charts] | [11.07] | [8.69] | [5.80] | [3.28] | | | | |

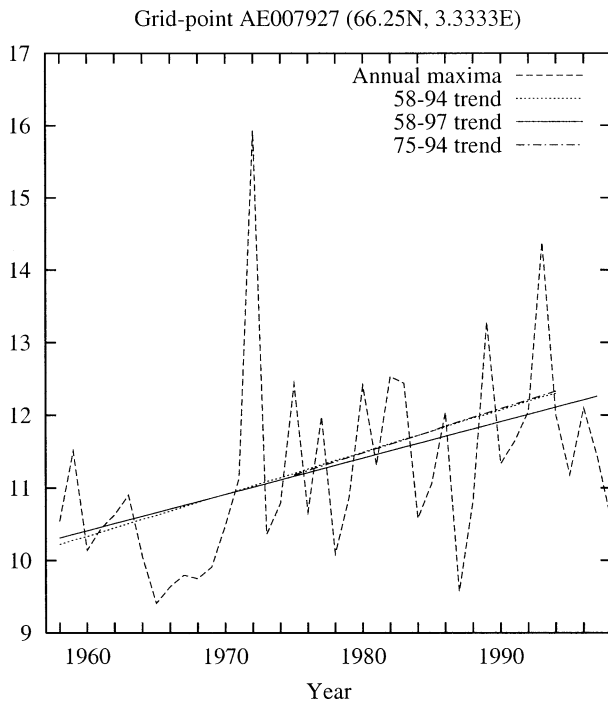


FIG. 3. Trends and time series of the annual maxima of SWH for grid point AE007927 (66.25°N, 3.3333°E), which is near the OWS Mike (66°N, 3°E).

The estimator of b proposed by Sen (1968), which is based on Kendall's rank correlation, was used in this study to estimate the slope b from the "prewhitened" time series W_t ; the Mann-Kendall test (Mann 1945; Kendall 1955) for randomness against trend is used to assess the significance of trend. Due to inevitable errors in the estimate of c , the prewhitening operation affects also any trend; however, the power of the test is reduced only weakly as long as c is not too large (von Storch and Navarra 1995). (Note that for the comparison described in section 2c, the trends presented were estimated without prewhitening the time series, which is more comparable to the simple linear regression used in the previous studies.)

When the Mann-Kendall test is carried out for each grid point in a grid separately, the rejection rate (i.e., the percentage of areas where the null hypothesis that the time series in question is random is rejected) is a measure of field significance of trend (Livezey and Chen 1983). Since the first 30 principal components (PCs) of the SWH extremes in question account for more than 95% of the total variance, the number of degrees of freedom of the fields is unlikely to exceed 30. According to Livezey and Chen (1983), for a field of 40, 30, and 20 degrees of freedom, one would expect, by accident, a rejection rate of about 12.5%, 13.5%, and 17.0%, respectively, if the test is conducted at the 5% significance level. Thus, the trend here could be field significant at the 5% level only if the rejection rate is greater than 12.5%. It should be pointed out that the aforementioned

field significance measure is very stringent; it does not resolve the spatial structure of the field. A well-organized trend pattern with a marginal rejection rate deserves further attention.

Redundancy analysis is also carried out in the present study to reveal the atmospheric circulation regimes that control the variability of ocean wave extremes. Redundancy analysis is a least squares technique that can be used to identify patterns of different fields (\mathbf{X} and \mathbf{Y}) that are linked through the regression model:

$$\hat{\mathbf{Y}} = \mu_{\mathbf{Y}} + \mathbf{C}_{\mathbf{YX}} \mathbf{C}_{\mathbf{XX}}^{-1} (\mathbf{X} - \mu_{\mathbf{X}}), \quad (2)$$

where $\hat{\mathbf{Y}}$ is a linear prediction of \mathbf{Y} , $\mu_{\mathbf{X}}$ and $\mu_{\mathbf{Y}}$ are the expected values of \mathbf{X} and \mathbf{Y} , respectively, and $\mathbf{C}_{\mathbf{XX}}$ and $\mathbf{C}_{\mathbf{YX}}$ are the covariance and cross-covariance matrices.

While maximizing the associated predictand \mathbf{Y} variance, redundancy analysis seeks to find a hierarchy of orthogonal predictand modes \mathbf{a}_j , which are actually the eigenmodes of the linear prediction $\hat{\mathbf{Y}}$, and associate them with the corresponding predictor patterns \mathbf{p}_j ($j = 1, 2, 3, \dots$). The temporal variation of the j th best predicted mode \mathbf{a}_j is referred to as the j th best predicted component (or predictand time series). The proportion of the total variance in \mathbf{Y} that is predicted by the linear prediction $\hat{\mathbf{Y}}$ is called the redundancy index, denoted as $R^2(\mathbf{Y}; \hat{\mathbf{Y}})$. Details about redundancy analysis can be found in Wang and Swail (2001), Wang and Zwiers (2001), von Storch and Zwiers (1999), and Tyler (1982).

Here, the use of redundancy analysis is reasonable despite the local non-Gaussian behavior of the SWH extremes. This is due to the fact that the large-scale variability of the SWH field, as captured in the retained leading PCs (cf. section 3b) is not significantly non-Gaussian, as evaluated by the Kolmogorov-Smirnov test.

b. Procedures

First, we compress the datasets of huge dimension by projecting them onto a few representative empirical orthogonal functions (EOFs) thereby obtaining the representative PCs of the datasets. For each season, we estimated the EOFs of the SWH and SLP data separately, taking into account the effect of different sizes of grid boxes at different latitudes. To decide the number of leading EOFs/PCs to retain, we consider the length of the field time series in question, and look at the relevant spectrum of eigenvalues [trying to truncate modes at the last clear break in the slope of each eigenvalue curve; the rule of North et al. (1982) is also referenced]. We also tried with different EOF truncations and found that the main results are not sensitive to the EOF truncation when we retain the leading 7–10 EOFs/PCs. Thus, we decided to retain 7 leading EOFs/PCs for each season. Note that the number of leading EOFs/PCs retained in WS01 was also 7 for each season. However, the variance proportion of the SWH extremes associated with the 7 retained EOFs/PCs for each season is a little

larger in the Atlantic hindcast than in the global hindcast. This is due to the higher resolution of the former. The SWH variability of smaller scales resolved in the detailed Atlantic hindcast is to be analyzed in our future studies.

For each season, we then use the retained PCs of the SWH statistics (90th and 99th percentiles) as the predictand Y , and the retained SLP PCs as the predictor X , for the subsequent redundancy analysis. The regression model in redundancy analysis is trained using “detrended” SLP and SWH data for the 40-yr period (1958–97). That is, prior to fitting the regression model, we detrend the retained leading PCs of SWH and SLP if they are found to have a trend of statistical significance at 20% level. (Trends of lower than 80% confidence can be considered as trivial and trying to remove them could introduce unnecessary biases to the time series.) The statistical “predictions” are then produced by feeding the undetrended leading PCs of SLP to the regression model. The predictions are cross validated by withholding data for years $(i - 1)$, i , $(i + 1)$ when predicting year i . The resulting predictor and predictand modes (in the EOF space) are then converted back to the physical space by using the relevant retained EOFs.

In addition to the 40-yr NRA SLP data, the 99-yr (1899–1997) SLP data taken from NCAR dataset ds010.1 (Trenberth and Paolino 1980) were also used in this study, to estimate the seasonal SWH statistics for the whole century back to 1899. Because the ds010.1 SLP dataset has a much coarser spatial resolution than the NRA SLP, we repeated all steps of the redundancy analysis with this 99-yr SLP dataset and then do the cross-validated hindcast for the 99-yr period (the hindcast for years from 1899 to 1957 is based on the same regression model as for year 1958).

4. Changes in Atlantic Ocean wave extremes

In the present study, significant trends indicate trends identified at the 5% statistical significance level, unless otherwise specified. Areas of significant changes are hatched in the related figures. The rates of changes are given in cm yr^{-1} . Also, the changes in “% yr^{-1} ” refer to the changes expressed as percentages of the relevant 40-yr mean.

The main results of trend analysis on the seasonal 90th and 99th percentiles of significant wave height (H_{90} and H_{99}) are shown in Figs. 4 and 5. Generally, increases of SWH are found to be most significant in winter (JFM), and least significant in spring (AMJ). For winter H_{90} statistically significant increases are found over about 20% area of the northern North Atlantic (cf. Table 3).

For the winter seasonal 90th percentiles H_{90} , as shown in Fig. 4a, statistically significant increases of $2\text{--}6 \text{ cm yr}^{-1}$ (or $0.4\%\text{--}1.2\% \text{ yr}^{-1}$) are detected for the northeast North Atlantic, matched by significant decreases ($1\text{--}3.5 \text{ cm yr}^{-1}$) in the subtropical North Atlantic. When com-

pared with the trend pattern identified from the global hindcast (see Fig. 4b), significant increases (the hatched areas) are now less extensive, with the North Sea and the region off the Scandinavian coast now having lower rates of increase (showing a much smaller area of $4\text{--}5 \text{ cm yr}^{-1}$ increases; see the pink-shaded areas). The Atlantic hindcast shows increases of $1\text{--}4 \text{ cm yr}^{-1}$ for most of the North Sea. However, the rate of increase is a little greater for the region just north of Ireland, with the upper bound increasing from 5.1 cm yr^{-1} in the global hindcast to 6 cm yr^{-1} in the Atlantic hindcast; increases of $4\text{--}6 \text{ cm yr}^{-1}$ (the pink-shaded area) now cover an area larger than the area of $4\text{--}5.1 \text{ cm yr}^{-1}$ increases in the global hindcast. Also, the area of significant decreases (of $1\text{--}2 \text{ cm yr}^{-1}$) in the western part of subtropical North Atlantic is larger in the Atlantic hindcast than in the global hindcast.

In the spring season, however, differences between the Atlantic hindcast and the global hindcast are minor: both hindcasts have the lowest rejection rate for this season, showing only a small area of significant decreases in the southwest corner of the North Atlantic and in the ocean off the African coast (not shown).

In summer, the trend pattern is characterized by significant increases of $1\text{--}2 \text{ cm yr}^{-1}$ (or $0.4\text{--}0.7\% \text{ yr}^{-1}$) in the region off the Canadian coast (cf. Fig. 4c). The area of significant increase is much larger than its counterpart in the global hindcast, while the increasing trend in the subtropical North Atlantic (around 30°N) found from the global hindcast is not identified now (cf. Figs. 4c and 4d).

For the fall season, the trend pattern is also similar to the one identified from the global hindcast. However, as shown in Figs. 4e and 4f, the changes in the central North Atlantic are more significant in the Atlantic hindcast, with significant increases (of $1\text{--}3.4 \text{ cm yr}^{-1}$ or $0.4\text{--}0.8\% \text{ yr}^{-1}$) extending westward toward the Canadian coast, while the increases in the region southwest of Iceland are found to be much less significant.

Linear trends detected for the 99th percentiles (H_{99}) are generally less extensive than those for the 90th percentiles (H_{90}). For instance, the area of significant trends for winter H_{99} is just about half of that for its H_{90} counterpart (cf. Table 3). The trend pattern of winter H_{99} is similar to the one identified from the global hindcast (cf. Figs. 5a and 5b): significant increases in the northeast North Atlantic are still matched by significant decreases in the subtropical North Atlantic. However, the rates of increases are greater in the Atlantic hindcast: the significant increases are $5\text{--}8.5 \text{ cm yr}^{-1}$ (or $0.4\text{--}1.0\% \text{ yr}^{-1}$) for the region off the Scandinavian coast, and $4\text{--}7.5 \text{ cm yr}^{-1}$ ($0.4\text{--}0.9\% \text{ yr}^{-1}$) for the region northwest of Ireland; while the decreases in the western subtropical North Atlantic are $3\text{--}5.6 \text{ cm yr}^{-1}$ (or $0.5\text{--}0.9\% \text{ yr}^{-1}$).

For both spring and summer H_{99} the rejection rate is about 5% or less, which is not field significant. The trend patterns show no significant changes of well-organized structure.

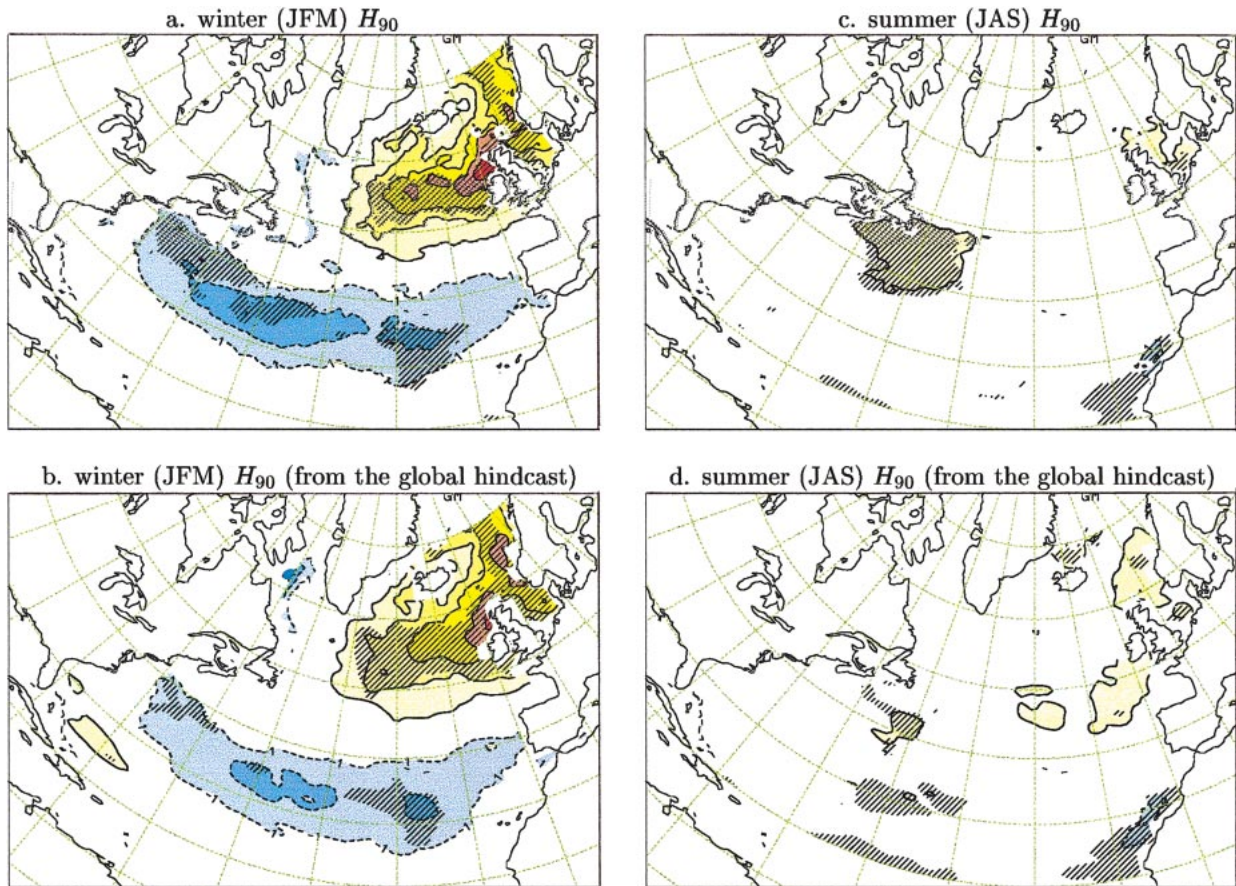


FIG. 4. (a), (c), (e) Changes (cm yr^{-1}) of the seasonal 90th percentiles of SWH (H_{90}) in the indicated seasons. The contour interval is 1 cm yr^{-1} . Solid and dashed lines are positive and negative contours respectively (zero contours are not drawn). Hatching indicates areas of significant changes. (b), (d), (f) The same as in (a), (c), (e) but for changes of the seasonal H_{90} as identified from the global wave hindcast using the NCEP reanalyzed wind fields (cf. WS01).

For the fall season H_{99} , the Atlantic hindcast results in a trend pattern that is similar to the one identified from the global hindcast. In the Atlantic hindcast, however, the increases in the region off the Canadian coast are much more significant ($4\text{--}7.5$ vs $2\text{--}4 \text{ cm yr}^{-1}$ in the global hindcast), while the increases in the northeast North Atlantic become insignificant (cf. Figs. 5c and 5d). Also, the fall H_{99} in the region just off the Canadian coast (Nova Scotia) appears to experience much higher rates of increase than its H_{90} counterpart (cf. Figs. 4e and 5c). In particular, the area of significant increases is located much closer to the Canadian coast for the H_{99} than for the H_{90} . These suggest that the region just off the Canadian coast has experienced higher extremes of ocean waves in the fall season of the last four decades, with significant increases of $4\text{--}7.5 \text{ cm yr}^{-1}$ (or $0.5\text{--}1.0\% \text{ yr}^{-1}$) being identified for the seasonal 99th percentiles while having little significant changes in the 90th percentiles. This is most likely due to the occurrence during the decade of the 1990s of the most severe wave-producing storm in the Northwest Atlantic, namely the “Halloween storm” of October 1991, and the better

representation in general of tropical storms in the Atlantic hindcast. The Halloween storm in particular shifts the 99th percentile value significantly upward, without greatly influencing the 90th percentile value.

The technique of trend analysis was also applied to the seven leading PCs of the seasonal wave extremes for each season. As in WS01, the results corroborate that trends of the SWH extremes (H_{90} and H_{99}) are most significant in winter. As partly shown in Fig. 6 (figures for winter H_{99} are similar and are hence not shown here), the EOF1 of winter H_{90} (H_{99}) resembles the relevant trend pattern shown in Fig. 4a (Fig. 5a), while the associated PC1 possesses a significant increasing trend, representing significant increases in the northeast North Atlantic matched by significant decreases in the subtropical North Atlantic. In other words, the EOF1/PC1 of winter H_{90} (H_{99}) well represents its trend component.

Significant trends are also identified for PC6 of spring H_{90} , for PC4 of summer H_{90} , and for PC3s of fall H_{90} and H_{99} . The PC6 of spring H_{90} explains only about 3.6% of the total interannual variance and is related to decreases in the subtropical North Atlantic. The trend

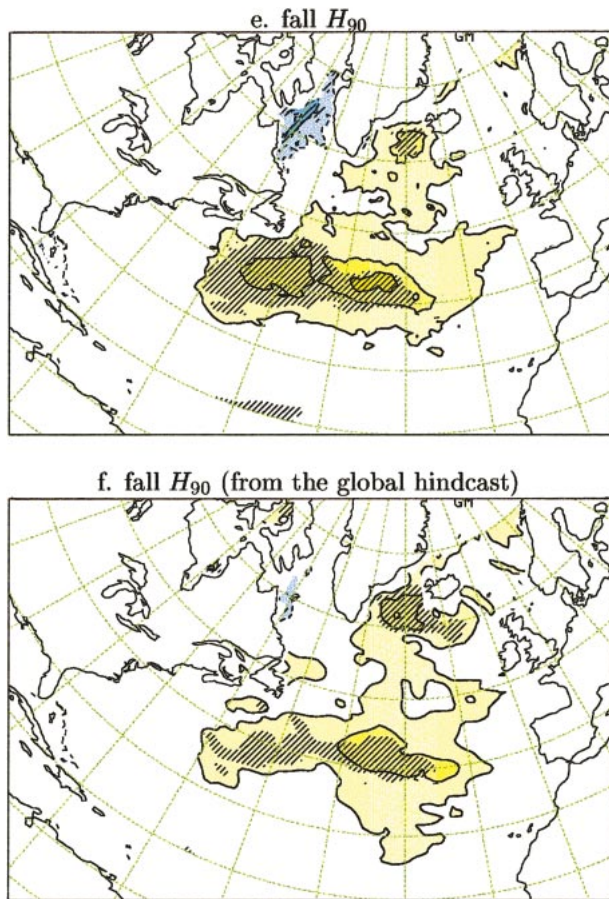


FIG. 4. (Continued)

component of fall H_{90} (or H_{99}) is well represented by the EOF3/PC3, and the trend component of summer H_{90} , by the EOF4/PC4. These EOFs (not shown) resemble the corresponding trend patterns.

In terms of the whole last century 1899–1997, however, changes are found to be insignificant. As shown in Fig. 7, the significant upward trend in the last four decades is matched by a significant downward trend in the first half of the century. This is consistent with the results of previous studies (WS01 and the WASA group).

5. Homogeneity of the wave data

In order to assess the degree of temporal homogeneity of the wave data from the Atlantic hindcast, we use the RA regression model, trained with detrended NRA SLP and SWH data, to predict SWH extremes using the undetrended NRA SLP data. Consistency of trends in the RA-predicted SWH extremes with the corresponding ones estimated directly from the Atlantic (numerical) hindcast suggest that the wave data are of the same degree of temporal homogeneity as the NRA SLP data.

Basically, the trends in the RA-predicted SWH ex-

TABLE 3. Percentages of areas with significant (at 5% level) changes in the seasonal 90th and 99th percentiles of SWH over subtropical North Atlantic (sNA: 20°–40°N), northern North Atlantic (nNA: 40°–70°N), and the whole North Atlantic (NA: 20°–70°N).

| | 90th percentiles | | | 99th percentiles | | |
|--------|------------------|------|------|------------------|------|-----|
| | sNA | nNA | NA | sNA | nNA | NA |
| Winter | 13.4 | 19.6 | 16.3 | 7.9 | 11.8 | 9.8 |
| Spring | 16.4 | 3.2 | 10.0 | 9.0 | 1.4 | 5.3 |
| Summer | 9.0 | 10.3 | 9.6 | 3.8 | 3.4 | 3.6 |
| Fall | 9.1 | 11.8 | 10.5 | 3.7 | 7.1 | 5.4 |

tremes are consistent with the raw (numerically hindcasted) SWH extremes, except that the raw data show a slightly lower rate of change. For example, as shown in Fig. 6b, the trend of the RA-predicted PC1 (the dashed straight line) is basically consistent with the trend of the raw (numerically hindcasted) PC1 (the solid straight line). The slope parameter is 1.51 for the raw PC1, and 1.57 for the predicted PC1. This indicates that, for the northeast North Atlantic, the increases of winter 90th percentiles are about 3.0–5.6 cm yr^{-1} for the raw SWH data, and about 3.1–5.8 cm yr^{-1} for the RA-predicted SWH data. [Note that the EOF1 has values of 0.020–0.037 in the northeast North Atlantic of significant increases, see Fig. 6a. These values multiplied by the slope is the rate of change in m yr^{-1} . Also, remember that the winter trend component of H_{90} (H_{99}) is well represented by the EOF1/PC1.] For the winter 99th percentiles, the slope parameter is 1.63 for the raw PC1, and 1.84 for the RA-predicted PC1 (not shown). We consider that such differences are insignificant, especially with the fact that the raw data have a lower rate of change. (It has been noticed that extreme storms tend to be underestimated in the first half of the century when only ship observations were available, because ships always try to avoid extreme storms.) There is no evidence that the kinematic reanalysis of wind fields compromised the homogeneity for the improvement in accuracy.

6. Association of atmospheric circulation with ocean wave

In this study, redundancy analysis is used to associate variations of ocean wave extremes with large-scale atmospheric circulation (SLP) regimes. For each variable in each season, Table 4 gives the percentages of the total variance associated with the corresponding retained leading EOFs/PCs.

Figure 8 shows the most important pair of the predictand (H_{90}) and predictor (seasonal mean SLP) modes in winter, as well as their temporal variations, which accounts for about 40% and 36% of the total predictand and predictor variance, respectively. Apparently, the best-predicted (H_{90}) mode resembles the trend pattern shown in Fig. 4a, and the predictor (NRA SLP) mode has a structure like the NAO. The predictor and pre-

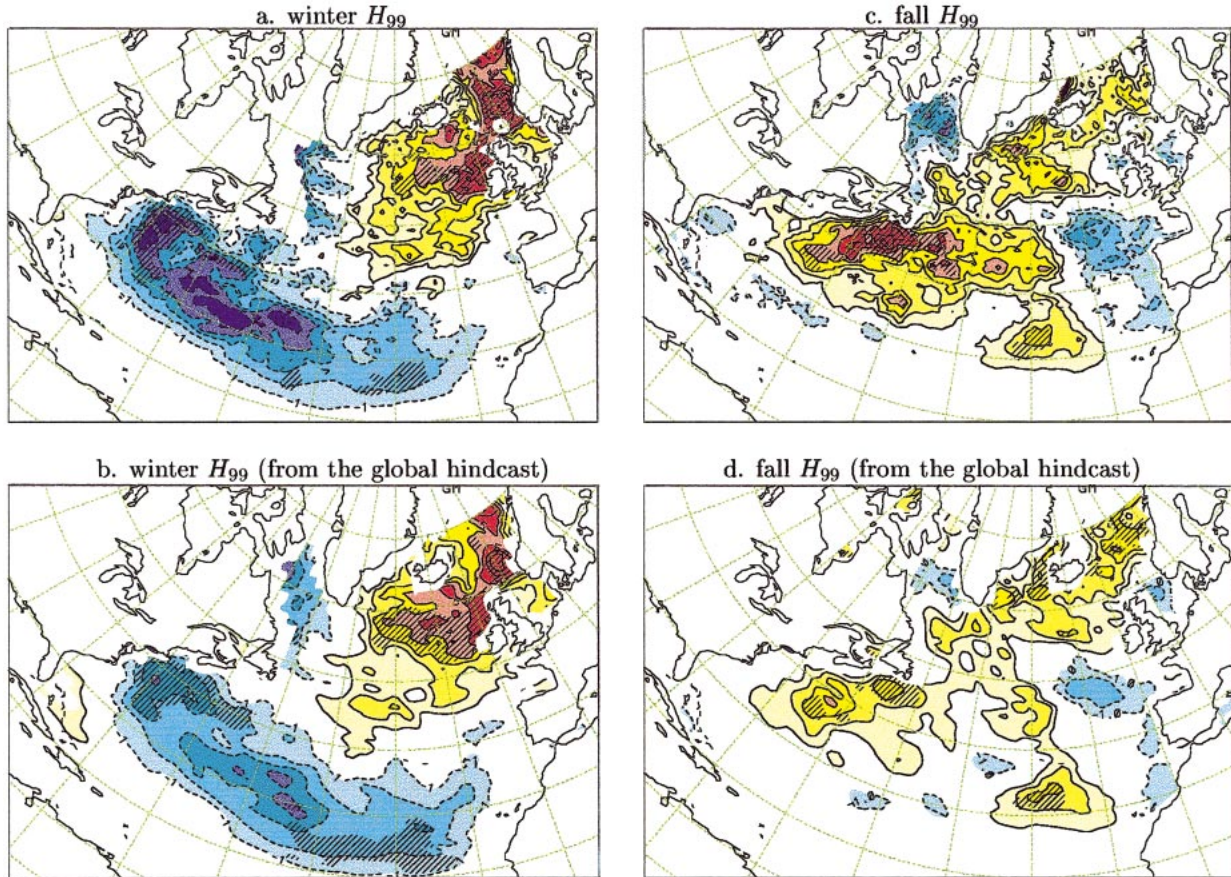


FIG. 5. The same as in Fig. 4 but for changes of the seasonal 99th percentiles of SWH (H_{99}) in the winter (JFM) and fall (OND) seasons.

dictand time series (i.e., SLP-T1 and H90-T1 in Fig. 8c) are highly correlated to each other (cf. Table 4), and both possess a significant increasing trend. These indicate that the Icelandic low has deepened during the

recent decades while the Azores high intensified, and in the meantime, extremes of SWH in the northeast North Atlantic have increased, accompanied by decreases of SWH extremes in the subtropical North Atlantic.

TABLE 4. The percentages of the total variance in the SWH extremes (P_{SWH}) or in the SLP fields (P_{SLP}) that are associated with the seven retained EOFs for each season, as well as the overall redundancy index, $R = R^2(\mathbf{Y}:\hat{\mathbf{Y}})$, and the redundancy indices associated with the j th best-predicted modes, $R_j = R^2(\mathbf{Y}:\mathbf{a}_j\hat{\mathbf{Y}})$. The numbers in square brackets are the correlations between the relevant pair of predictor and predictand time series (the 5% critical value is 0.312).

| | P_{SLP} | | P_{SWH} | R | R_1 | R_2 | R_3 | R_4 | R_5 | R_6 | R_7 |
|-----|-----------|----------|-----------|-------|---------|---------|---------|---------|---------|---------|---------|
| JFM | 94.0 | H_{90} | 84.6 | 0.872 | 0.517 | 0.197 | 0.075 | 0.050 | 0.017 | 0.013 | 0.004 |
| | | H_{99} | 70.6 | 0.682 | 0.390 | 0.151 | 0.067 | 0.037 | 0.020 | 0.009 | 0.008 |
| AMJ | 81.1 | H_{90} | 72.7 | 0.526 | 0.295 | 0.114 | 0.070 | 0.030 | 0.010 | 0.015 | 0.003 |
| | | H_{99} | 65.5 | 0.506 | 0.273 | 0.081 | 0.064 | 0.056 | 0.014 | 0.013 | 0.005 |
| JAS | 85.8 | H_{90} | 73.5 | 0.466 | 0.161 | 0.155 | 0.073 | 0.038 | 0.017 | 0.015 | 0.006 |
| | | H_{99} | 65.3 | 0.388 | 0.206 | 0.067 | 0.049 | 0.026 | 0.016 | 0.013 | 0.012 |
| OND | 90.9 | H_{90} | 78.3 | 0.749 | 0.385 | 0.214 | 0.073 | 0.035 | 0.022 | 0.015 | 0.006 |
| | | H_{99} | 64.0 | 0.554 | 0.217 | 0.182 | 0.065 | 0.043 | 0.025 | 0.014 | 0.009 |
| | | | | | [0.950] | [0.831] | [0.771] | [0.671] | [0.005] | [0.290] | [0.014] |
| | | | | | [0.865] | [0.821] | [0.020] | [0.345] | [0.068] | [0.277] | [0.237] |
| | | | | | [0.794] | [0.661] | [0.615] | [0.313] | [0.237] | [0.035] | [0.088] |
| | | | | | [0.723] | [0.391] | [0.318] | [0.484] | [0.128] | [0.068] | [0.054] |
| | | | | | [0.020] | [0.100] | [0.225] | [0.351] | [0.016] | [0.123] | [0.023] |
| | | | | | [0.630] | [0.468] | [0.378] | [0.315] | [0.161] | [0.071] | [0.020] |
| | | | | | [0.878] | [0.881] | [0.770] | [0.253] | [0.378] | [0.026] | [0.018] |
| | | | | | [0.780] | [0.733] | [0.593] | [0.063] | [0.189] | [0.084] | [0.31] |

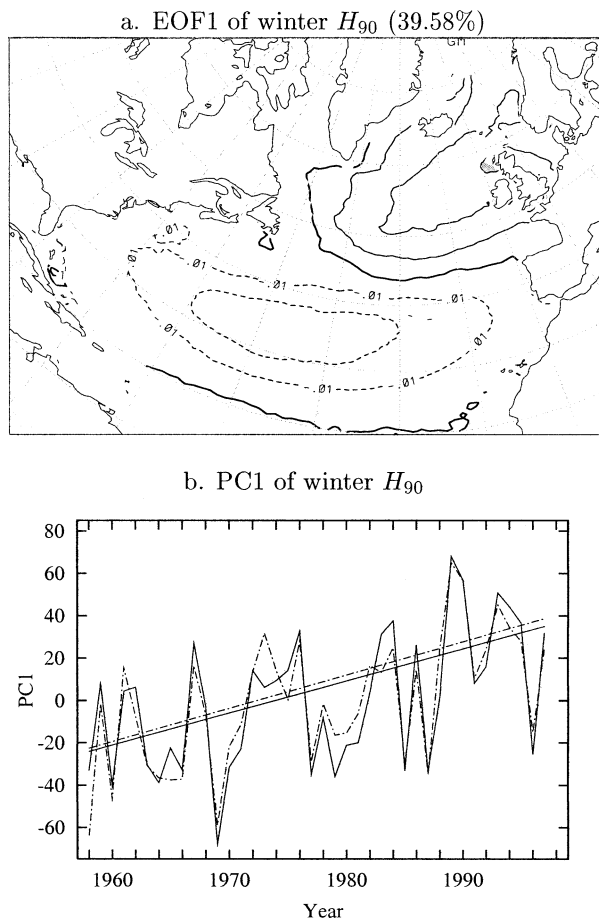


FIG. 6. The EOF1 and PC1 of winter (JFM) seasonal 90th percentiles of SWH (H_{90} , in m). (a) The contour interval is 0.01; solid, bold, and dashed lines are positive, zero, and negative contours, respectively. The number in parentheses is the percentage of variance explained by the EOF. (b) The solid curve represents the PC1 of the numerical hindcast, and the dashed curve, the PC1 of the statistical hindcast. The solid and dashed straight lines represent trends estimated from the solid and dashed curves, respectively.

Moreover, both the predictor and predictand time series are highly significantly correlated with the simultaneous NAO index (based on the difference of normalized SLP between Ponta Delgada, Azores, and Stykkisholmur/Reykjavik, Iceland; Hurrell 1995), the correlation being 0.98 and 0.93, respectively.

For the winter seasonal 99th percentiles H_{99} , similar results were obtained: the best predicted (H_{99}) mode resembles the relevant trend pattern, and the associated predictor (SLP) mode has an NAO-like structure (not shown). Both the predictor and predictand time series possess a significant increasing trend, and both series are significantly correlated with the NAO index (the correlation being 0.98 and 0.83, respectively). All these again clearly corroborate that changes of the winter SWH extremes in the recent decades are intimately associated with the NAO variability.

Changes of the seasonal 90th percentiles of SWH

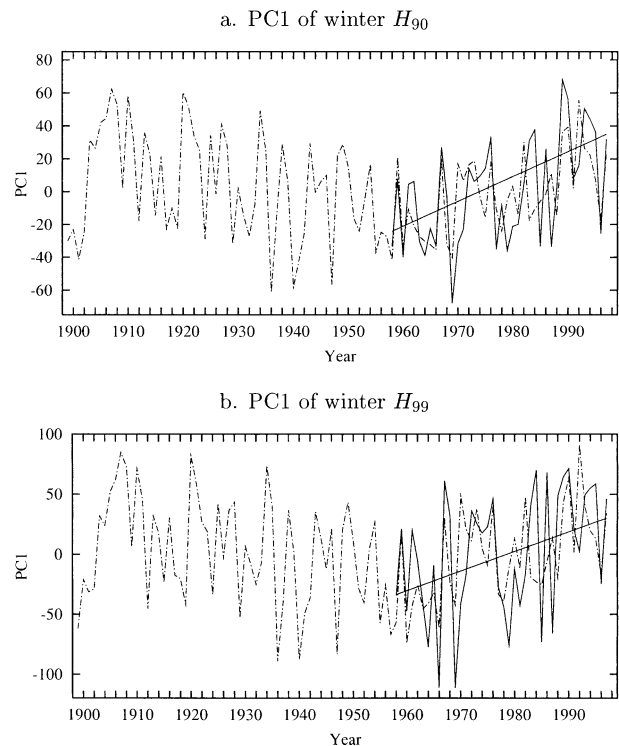


FIG. 7. The PC1s of winter (JFM) seasonal 90th and 99th percentiles of SWH (H_{90} , H_{99} , in m). The solid curves represent the PC1s of the numerical hindcast, and the dashed curves, the PC1s of the statistical reconstruction using SLP from the NCAR dataset ds010.1 (Trenberth and Paolino 1980). The trend lines are estimated from the solid curves.

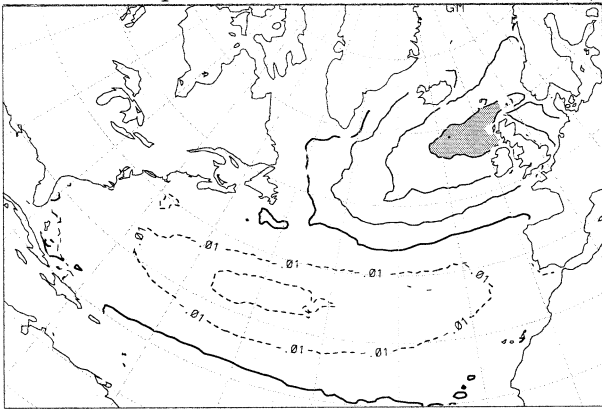
(H_{90}) in the fall season are also closely linked with changes in the NRA SLP field. Such a relationship is represented by the third pair (rather than the first pair) of predictor (SLP) and predictand (H_{90}) modes, which indicates that the changes are not as overwhelming as those in the winter season. Specifically, as shown in Fig. 9, significant increases of fall H_{90} in the central North Atlantic are associated with an anomalous low pressure over the region, which is matched by an anomalous high pressure over Europe. A similar link is also found between the SLP field and the fall H_{99} . These relationships between the SWH extremes and SLP in the fall season are not as apparent in the global hindcast (cf. WS01).

In the summer season, the relationship between SLP and SWH is much weaker. No significant SLP changes were found to be linked to the marginally significant changes in the summer H_{90} .

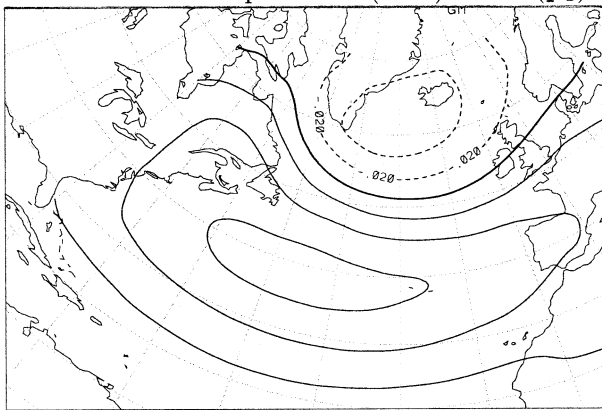
7. Summary

In this study, the seasonal extremes of significant wave height (SWH) in the North Atlantic are analyzed. The analysis is based on a 40-yr numerical hindcast using kinematically reanalyzed wind fields. Changes in the ocean wave extremes are identified by performing the Mann–Kendall test and are further related to changes

a. the best-predicted mode of winter H_{90} (\mathbf{a}_1)



b. the associated predictor (SLP) mode (\mathbf{p}_1)



c. Temporal variations of modes \mathbf{a}_1 and \mathbf{p}_1

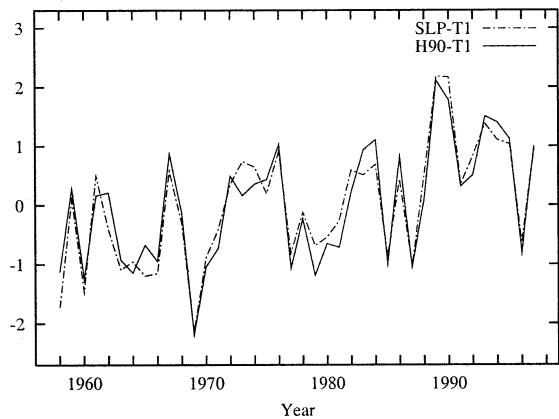
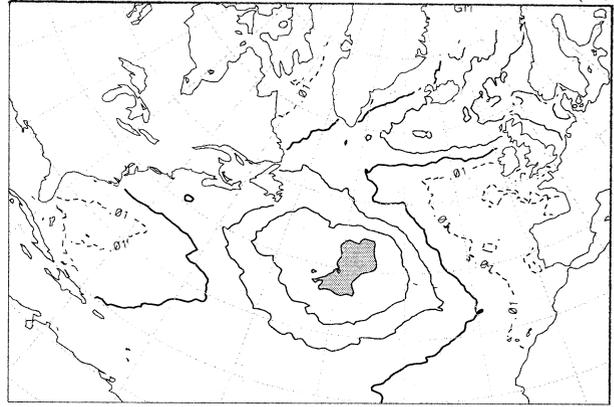
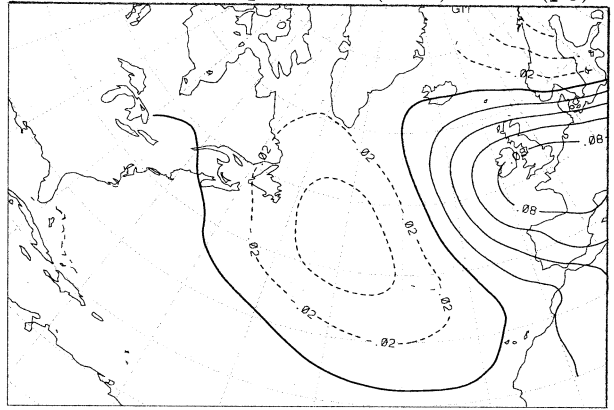


FIG. 8. The best predicted mode of seasonal 90th percentiles of SWH (H_{90}) and the associated predictor (SLP) mode in winter (JFM). Both the predictor and the predictand time series (SLP-T1 and H90-T1; normalized) have a significant increasing trend.

a. the third best-predicted mode of fall H_{90} (\mathbf{a}_3)



b. the associated predictor (SLP) mode (\mathbf{p}_3)



c. Temporal variations of modes \mathbf{a}_3 and \mathbf{p}_3

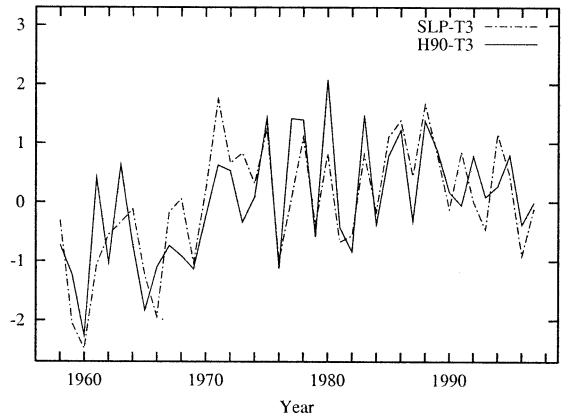


FIG. 9. The third best-predicted mode of seasonal 90th percentiles of SWH (H_{90}) and the associated predictor (SLP) mode in fall (OND). Both the predictor and the predictand time series (SLP-T3 and H90-T3; normalized) have a significant increasing trend.

in the atmospheric circulation (SLP) by means of redundancy analysis.

The results show that in the last four decades changes of SWH extremes are most significant in the winter

season, with little significant change being found in the spring season. In winter, the changes of SWH extremes are closely associated with changes in the NAO variability. More specifically, significant increases of SWH

extremes in the northeast North Atlantic are closely related to the deepening of the Icelandic low and the strengthening of the Azores high during the last four decades. In the fall season, some changes are also found to be statistically significant and linked with significant changes in the atmospheric circulation at the sea level. Not surprisingly, increases of ocean wave height are generally associated with anomalous low pressure over the region.

Linear trends detected for the 99th percentiles of SWH are generally less extensive than those for the 90th percentiles counterpart. However, it is worth noting that some significant increases are detected in the region just off the Canadian coast in the fall for the 99th percentiles but not for the 90th percentiles. This indicates that this oceanic area there has roughened in this season during the last four decades, experiencing higher wave extremes. The "Halloween storm" of October 1991 is a typical case of this kind.

Generally speaking, both the detailed Atlantic wave hindcast and the global wave hindcast show similar trend patterns and their links to the large-scale atmospheric circulation. However, with the higher spatial resolution, the Atlantic hindcast shows more clearly the profound connection between the variability of SWH extremes and the large-scale atmospheric circulation. When compared with the global wave hindcast (cf. WS01), generally, the Atlantic wave hindcast shows more significant increases in the region off the Canadian coast in summer and fall, and in winter it shows higher rates of increases in the region northwest of Ireland but less significant changes in the North Sea and in the region off the Scandinavian coast. Also, in the Atlantic hindcast, a larger area of significant decreases of SWH extremes is observed in the western part of the subtropical North Atlantic in winter. The differences found in the midlatitude and subtropical North Atlantic result from the necessary adjustment of wind fields for tropical cyclones and extratropical storms in the kinematic reanalysis of wind fields.

Acknowledgments. The authors would like to acknowledge the considerable efforts of Dr. V. J. Cardone and the meteorologists at Oceanweather, Inc., in the preparation of the kinematically analyzed wind fields that are the core of the high-quality wave hindcast; in particular, Andrew Cox, Liz Ceccacci, and Brian Callahan. The authors are also grateful to Ain Niitsoo for some of the statistical analysis of the hindcast data, and managing the extremely large databases involved. Dr. Xuebin Zhang offered helpful suggestions and discussions during the course of this study, which are greatly appreciated. The authors greatly appreciate Dr. Francis Zwiers's helpful comments on an earlier version of this manuscript. The two reviewers' comments/suggestions are also acknowledged.

APPENDIX

Description of OWI-3G Wave Model

The OWI-3G wave model used for this hindcast is a discrete spectral type. The spectrum is resolved at each grid point in 24 directional bins and 23 frequency bins. The bin center frequencies range from 0.039 to 0.32 Hz increasing in geometric progression with a constant ratio 1.100 64. Deepwater physics is assumed in both the propagation algorithm and the source terms. The propagation scheme (Greenwood et al. 1985) is a downstream interpolatory scheme that is rigorously energy conserving with great circle propagation effects included. The source term formulation and integration is a third-generation type (WAMDI Group 1988) but with different numerics and with the following modifications of the source terms in official WAMDI. First, a linear excitation source term is added to the input source term to allow the sea to grow from a flat calm condition without an artificial warm start sea state. The exponential wind input source is taken as the Snyder et al. (1981) linear function of friction velocity, as in WAMDI. However, unlike WAMDI, in which friction velocity is computed from the input 10-m wind speed following the drag law of Wu (1982), a different drag law is used in OWI-3G. That law follows Wu closely up to wind speed of 20 m s^{-1} and then becomes asymptotic to a constant at hurricane wind speeds. The wave model then appears to produce a more realistic wave growth, since the drag coefficient tends to converge slowly to a limiting value as the wind speed becomes more extreme (Khandekar et al. 1994). The dissipation source term is taken from WAMDI except that the frequency dependence is cubic rather than quadratic. Finally, the discrete interaction approximation to the nonlinear source term is used as in WAMDI except that two modes of interaction are included (in WAMDI the second mode is ignored). Further details on this model and its validation may be found in Khandekar et al. (1994), Cardone et al. (1996), and Forristall and Greenwood (1998).

In the Atlantic hindcast described here, OWI-3G is adapted on a latitude-longitude grid consisting of a $122 (\text{lat}) \times 126 (\text{lon})$ array of points. The grid spacing is $0.625^\circ \text{ lat} \times 0.833^\circ \text{ lon}$, which is within 10% of square (i.e., $\Delta x = \Delta y$) between 38° and 45°N . The eastern boundary is at 20°E and the northern boundary is at 75.625°N . There are 9023 grid points. The south edge of the grid is at the equator. This boundary was treated as open; wave spectra interpolated from the output of a lower resolution (2.5° at a 3-h time step) global second-generation model driven by unmodified NRA 10-m wind fields (Cox and Swail 2001) are used as boundary conditions along the equator to preserve South Atlantic swells. The basic model integration time step is 0.5 h and consists of one 30-min propagation time step and two 15-min growth cycles.

Ice cover was specified for each month from mid-

monthly ice tables specified on the wave grid from Walsh and Johnson (1979; prior to 1972), Arctic and Antarctic sea ice data CD-ROM 1972–94, and hand-digitized maps produced from the joint Navy/NOAA Ice Center datasets. The 5/10 ice concentration contour was used as the definition of the ice edge—points with ice concentrations greater than 5/10 were considered as land by the model, those with concentrations 5/10 or less were considered as open water.

The output of the model consists of 17 “field” quantities (e.g., significant wave height, peak period, vector mean direction, partitioned fields, directional and angular spreading) at all grid points and the full two-dimensional spectrum at 233 grid points. The spectral save points were selected to allow even coverage of the basin (every 5° of lat and lon), as well as to allow the possibility to drive finer mesh models for the U.S. east coast, the Scotian shelf, and Grand Banks of Newfoundland and the European west coast. Spectra were also saved at the locations of selected moored buoys and offshore platforms.

REFERENCES

- Bacon, S., and D. J. T. Carter, 1991: Wave climate changes in the North Atlantic and North Sea. *Int. J. Climatol.*, **11**, 545–558.
- , and —, 1993: A connection between mean wave height and atmospheric pressure gradient in the North Atlantic. *Int. J. Climatol.*, **13**, 423–436.
- Bouws, E., D. Jannink, and G. J. Komen, 1996: The Increasing wave height in the North Atlantic Ocean. *Bull. Amer. Meteor. Soc.*, **77**, 2275–2277.
- Cardone, V. J., J. G. Greenwood, and M. A. Cane, 1990: On trends in historical marine wind data. *J. Climate*, **3**, 113–127.
- , A. T. Cox, J. A. Greenwood, and E. F. Thompson, 1994: Upgrade of tropical cyclone surface wind field model. U.S. Corps of Engineers Misc. Paper CERC-94-14, 97 pp.
- , H. C. Graber, R. E. Jensen, S. Hasselmann, and M. J. Caruso, 1995: In search of the true surface wind field in SWADE IOP-1: Ocean wave modeling perspective. *Global Ocean Atmos. Syst.*, **3**, 107–150.
- , R. E. Jensen, D. T. Resio, V. R. Swail, and A. T. Cox, 1996: Evaluation of contemporary ocean wave models in rare extreme events: The “Halloween Storm” of October 1991 and the “Storm of the Century” of March 1993. *J. Atmos. Oceanic Technol.*, **13**, 198–230.
- Carter, D. J. T., and L. Draper, 1988: Has the north-east Atlantic become rougher? *Nature*, **332**, 494.
- Cotton, P. D., and D. J. T. Carter, 1994: Cross calibration of TOPEX, ERS-1, and GEOSAT wave heights. *J. Geophys. Res.*, **99**, 25 025–25 033.
- Cox, A. T., and V. R. Swail, 2001: A global wave hindcast over the period 1958–1997: Validation and climate assessment. *J. Geophys. Res.*, **106** (C2), 2313–2329.
- , J. A. Greenwood, V. J. Cardone, and V. R. Swail, 1995: An interactive objective kinematic analysis system. *Proc. Fourth Int. Workshop on Wave Hindcasting and Forecasting*, Downsview, ON, Canada, Environment Canada, 109–118.
- , V. J. Cardone, and V. R. Swail, 2001: On the use of in situ and satellite wave measurements for evaluation of wave hindcasts. *Guide to the Applications of Marine Climatology, Part II*, World Meteorological Organization, in press.
- Forristall, G. Z., and J. A. Greenwood, 1998: Directional spreading of measured and hindcasted wave spectra. *Proc. Fifth Int. Workshop on Wave Hindcasting and Forecasting*, Melbourne, FL, Environment Canada, 5–15.
- Gibson, R., P. Kallberg, and S. Uppala, 1996: The ECMWF Reanalysis (ERA) Project. *ECMWF Newsl.*, **73**, 7–17.
- Greenwood, J. A., V. J. Cardone, and L. M. Lawson, 1985: Inter-comparison test version of the SAIL wave model. *Ocean Wave Modelling*, Plenum Press, 221–233.
- Grevenmeyer, I., R. Herber, and H.-H. Essen, 2000: Microseismological evidence for a changing wave climate in the northeast Atlantic Ocean. *Nature*, **408**, 349–352.
- Gunther, H., W. Rosenthal, M. Stawarz, J. C. Carretero, M. Gomez, I. Lozano, O. Serano, and M. Reistad, 1998: The wave climate of the Northeast Atlantic over the period 1955–1994: The WASA wave hindcast. *Global Atmos. Ocean Syst.*, **6**, 121–163.
- Hurrell, J. W., 1995: Decadal trends in the North Atlantic Oscillation: Regional temperatures and precipitation. *Science*, **269**, 676–679.
- Kalnay, E., and Coauthors, 1996: The NCEP/NCAR 40-Year Reanalysis Project. *Bull. Amer. Meteor. Soc.*, **77**, 437–471.
- Kendall, M. G., 1955: *Rank Correlation Methods*. Charles Griffin, 196 pp.
- Khandekar, M. L., R. Lalbeharry, and V. J. Cardone, 1994: The performance of the Canadian Spectral Ocean Wave Model (CSOWM) during the Grand Banks ERS-1 SAR Wave Spectra Validation Experiment. *Atmos.–Ocean*, **32**, 31–60.
- Kushnir, Y., V. J. Cardone, J. G. Greenwood, and M. A. Cane, 1997: The recent increase in North Atlantic wave heights. *J. Climate*, **10**, 2107–2113.
- Livezey, R. E., and W. Y. Chen, 1983: Statistical field significance and its determination by Monte Carlo techniques. *Mon. Wea. Rev.*, **111**, 46–59.
- Mann, H. B., 1945: Non-parametric tests against trend. *Econometrica*, **13**, 245–259.
- North, G. R., L. B. Thomas, and R. F. Cahalan, 1982: Sampling error in the estimation of empirical orthogonal functions. *Mon. Wea. Rev.*, **110**, 699–706.
- Powell, M. D., and P. G. Black, 1990: The relationship of hurricane reconnaissance flight-level wind measurements to winds measured by NOAA’s oceanic platforms. *J. Wind Eng. Ind. Aerodyn.*, **36**, 381–392.
- Sen, P. K., 1968: Estimates of the regression coefficient based on Kendall’s tau. *J. Amer. Stat. Assoc.*, **63**, 1379–1389.
- Snyder, R., F. W. Dobson, J. A. Elliott, and R. B. Long, 1981: Array measurements of atmospheric pressure fluctuations above surface gravity waves. *J. Fluid Mech.*, **102**, 1–59.
- Sterl, A., G. J. Komen, and P. D. Cotton, 1998: Fifteen years of global wave hindcasts using winds from the European Centre for Medium-Range Weather Forecasts reanalysis: Validating the reanalyzed winds and assessing the wave climate. *J. Geophys. Res.*, **103** (C3), 5477–5492.
- Swail, V. R., and A. T. Cox, 2000: On the use of NCEP/NCAR reanalysis surface marine wind fields for a long-term North Atlantic wave hindcast. *J. Atmos. Oceanic Technol.*, **17**, 532–545.
- , M. Parsons, B. T. Callahan, and V. J. Cardone, 1995: A revised extreme wave climatology for the east coast of Canada. *Proc. Fourth Int. Workshop on Wave Hindcasting and Forecasting*, Downsview, ON, Canada, Environment Canada, 81–91.
- Thompson, E. F., and V. J. Cardone, 1996: Practical modeling of hurricane surface wind fields. *J. Waterway, Port, Coastal, Ocean Eng.*, **112**(4), 195–205.
- Trenberth, K. E., and D. A. Paolino Jr., 1980: The Northern Hemisphere sea-level pressure data set: Trends, errors and discontinuities. *Mon. Wea. Rev.*, **108**, 855–872.
- Tyler, D. E., 1982: On the optimality of the simultaneous redundancy transformations. *Psychometrika*, **47**, 77–86.
- von Storch, H., and A. Navarra, Eds., 1995: *Analysis of Climate Variability—Applications of Statistical Techniques*. Springer-Verlag, 334 pp.

- , and F. W. Zwiers, 1999: *Statistical Analysis in Climate Research*. Cambridge University Press, 484 pp.
- Walsh, J. E., and C. M. Johnson, 1979: An analysis of Arctic sea ice fluctuations, 1953–1977. *J. Phys. Oceanogr.*, **9**, 580–591.
- WAMDI Group, 1988: The WAM model—A third generation ocean wave prediction model. *J. Phys. Oceanogr.*, **18**, 1775–1810.
- Wang, X. L., and V. R. Swail, 2001: Changes of extreme wave heights in Northern Hemisphere oceans and related atmospheric circulation regimes. *J. Climate*, **14**, 2204–2221.
- , and F. W. Zwiers, 2001: Using redundancy analysis to improve dynamical seasonal mean 500 hPa geopotential forecasts. *Int. J. Climatol.*, **21**, 637–654.
- WASA Group, 1998: Changing waves and storms in the northeast Atlantic? *Bull. Amer. Meteor. Soc.*, **79**, 741–760.
- Woodruff, S. D., R. J. Slutz, R. L. Jenne, and P. M. Steurer, 1987: A comprehensive ocean–atmosphere data set. *Bull. Amer. Meteor. Soc.*, **68**, 1239–1250.
- Wu, J., 1982: Wind-stress coefficients over the sea surface from breeze to hurricane. *J. Geophys. Res.*, **87**, 9704–9706.